ACS APPLIED ENERGY MATERIALS

www.acsaem.org Article

Potential-Dependent Layering in the Electrochemical Double Layer of Water-in-Salt Electrolytes

Ruixian Zhang, Mengwei Han, Kim Ta, Kenneth E. Madsen, Xinyi Chen, Xueyong Zhang, Rosa M. Espinosa-Marzal,* and Andrew A. Gewirth*

Cite This: *ACS Appl. Energy Mater.* 2020, 3, 8086−8094 Read Online

ACCESS | Metrics & More | Article Recommendations | Supporting Information

ABSTRACT: Water-in-salt electrolytes (WiSE) are concentrated aqueous electrolytes recently developed that are of great interest because of their possible relevance for batteries. The origin for their promising application has been ascribed to the formation of percolating nanodomains in the bulk. However, the interfacial structure of WiSE still remains to be understood. In this paper, we characterize the potential-dependent double layer of a LiTFSI-based electrolyte on a charged electrode surface. Ultramicroelectrode (UME) measurements reveal a surface-confinement effect for a ferricyanide redox species at the electrode/WiSE interface. Potential-dependent atomic force microscopy (AFM) shows the presence of layers, the structure of which changes with the applied potential. Thicker layers (6.4 and 6.7 Å) are observed at positive potentials, associated with $[Li(H_2O)_x]^+([TFSI]^-)_y$ ion pairs, while thinner layers (2.8 and 3.3 Å) are found at negative potentials and associated with $[Li(H_2O)_x]^+$ alone. Vibrational spectroscopy shows that the composition of the double layer also changes with potential, where $[TFSI]^-$ is enriched at positive and $[Li(H_2O)_x]^+$ enriched at negative potentials.

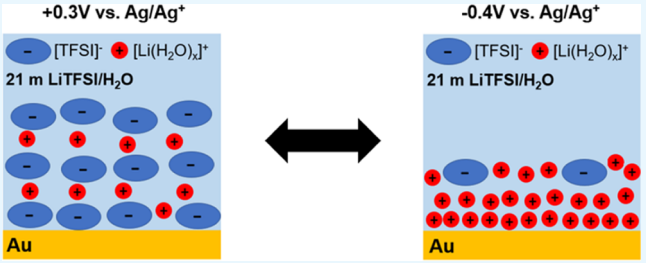

KEYWORDS: *aqueous electrolytes, double layer, batteries, atomic force microscopy, concentrated electrolytes*

INTRODUCTION

New electrolytes can enable new chemistries and opportunities for Li-based batteries.[1−3] Concentrated electrolytes have emerged as promising candidates.[4] These electrolytes contain a high salt-to-solvent ratio, as opposed to that of dilute electrolytes, and the number of free solvent molecules decreases due to coordination with Li^+ cations.[5,6] This high salt concentration and lack of free solvent molecules lead to improved electrolyte properties, such as faster Li^+ transport, an extended stability window, and a unique passivating solid-electrolyte interface (SEI).[7,8]

Among the concentrated electrolytes, water-in-salt electrolytes (WiSE) have attracted wide attention.[5,9] These electrolytes utilize H_2O as the solvent instead of flammable organic solvents. The addition of high-concentration lithium salts (including LiTFSI, LiOTF, LiFSI, etc.) allows coordination of H_2O molecules to Li^+ cations and produces a passivating SEI, which inhibits H_2O decomposition reactions and greatly expands the electrolyte stability window.[10,11] WiSE is considered a promising electrolyte for use in next-generation Li-ion batteries.

The electrical double layer formed by the WiSE at the solid−liquid interface is of great interest. Computational studies have investigated the change in the WiSE double layer with potential.[12−14] Molecular dynamics (MD) simulations suggest that H_2O is depleted from the double layer when the electrode surface is positively biased and enhanced when the electrode is negatively charged.[12] While substantial work investigates the bulk structure of WiSE and related electrolytes, experimental verification of the effect of potential on the double layer for WiSE is limited, with one surface-enhanced infrared absorption spectroscopy (SEIRAS) study on mixed WiSE consisting of 21 m LiTFSI and 7 m LiOTf to investigate the preferred anion comprising the double layer.[9,15,16] This paucity of work stands in contrast to the considerable experimental effort examining the electrochemical double layer in dilute aqueous electrolytes.[17,18] Therefore, a study on the electrical double layer of WiSE would be informative in terms of understanding the electrode−WiSE interface.

Atomic force microscopy (AFM) can be utilized to probe the double-layer structure with changing potential.[19,20] Prior studies used potential-dependent AFM on ionic liquids to show a layered double-layer structure varying with potential.[21]

Received: July 1, 2020
Accepted: July 28, 2020
Published: July 28, 2020

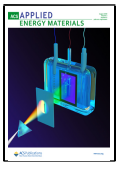

https://dx.doi.org/10.1021/acsaem.0c01534
ACS Appl. Energy Mater. 2020, 3, 8086−8094

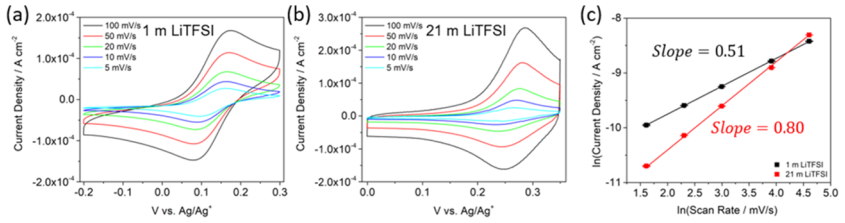

Figure 1. CVs obtained from a Au disk electrode (d = 0.875 cm) in 1 mM $K_3Fe(CN)_6$ in (a) 1 m LiTFSI and (b) 21 m LiTFSI at different scan rates, (c) the plot of ln(peak reduction current density) versus ln(scan rate) derived from corresponding CVs.

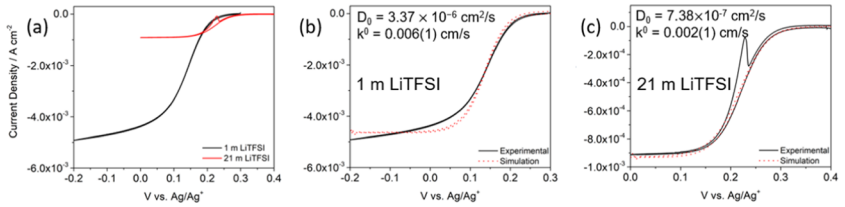

Figure 2. (a) Experimental CVs of 5 mM $K_3Fe(CN)_6$ in 1 m LiTFSI and 21 m LiTFSI at 2 mV/s using a Pt UME (d = 25 μm), and experimental and simulated CVs of 5 mM $K_3Fe(CN)_6$ in (b) 1 m LiTFSI and (c) 21 m LiTFSI.

AFM force curves also provide information on the composition of the double layer.[22,23]

The electrochemical behavior of small molecules in the WiSE is also of interest. The solvation environment of the WiSE system differs greatly from that of a dilute electrolyte, and its effect on processes including redox kinetics and diffusion remains to be explored.[5,9] Ultramicroelectrodes (UMEs) have been utilized to probe redox processes and would be useful in understanding the difference between WiSE and dilute electrolyte in terms of electrolyte interaction with redox species.[24−26]

In this work, we use AFM, UME, and vibrational spectroscopy to probe changes at an electrode/WiSE interface. A layered double-layer structure is observed on a (111) textured Au surface in AFM, and the layered structure and consequently surface excess of the electrolyte components vary with potential. Spectroscopy coupled with AFM illuminates the composition of the double layer at different potentials. $[TFSI]^-$ and $[Li(H_2O)_x]^+([TFSI]^-)_y$ clusters are the predominant species at positive potentials and $[Li(H_2O)_x]^+$ comprises the double layer at negative potentials. In addition, electrochemical characterization reveals the presence of a surface-confinement effect for a ferricyanide ($[Fe(CN)_6]^{3-}/[Fe(CN)_6]^{4-}$) redox couple, possibly due to interaction with the strongly layered WiSE structure.

RESULTS

Electrochemical Characterization. Figure 1a shows cyclic voltammograms (CVs) obtained from a Au disk electrode (d = 0.875 cm) immersed in a solution containing 1 mM $K_3Fe(CN)_6$ in 1 m LiTFSI at scan rates of 5, 10, 20, 50, and 100 mV/s. The CV curves show reduction peaks at 0.09 V and oxidation peaks at 0.15 V vs Ag/Ag^+, with a peak separation of 60 mV. The CVs correspond well to a diffusion-controlled reversible $[Fe(CN)_6]^{3-}/[Fe(CN)_6]^{4-}$ faradaic process with an E^0 = 0.12 V vs Ag/Ag^+.[27]

Figure 1b shows the CVs obtained from a Au electrode immersed in 1 mM $K_3Fe(CN)_6$ in 21 m LiTFSI at the same scan rates. The CV shows that the reduction and oxidation peaks are at 0.24 and 0.28 V, respectively. The resulting separation between the two peaks is 40 mV, which is smaller than the 57 mV separation expected for a diffusion-controlled reversible faradaic process.[27] The smaller peak separation is typically associated with a surface-confined reversible redox process.[28] The redox potential shifts to an apparent E^0 = 0.26 V, which could be due to a change in the solvation structure of $[Fe(CN)_6]^{3-}$ or a change in the Ag/Ag^+ reference potential. Little discussion attends changes in this reference potential in highly concentrated electrolytes such as that used here. The use of an additional test redox couple is similarly complicated. A Ag pseudoelectrode has been reported to exhibit little potential drift in nonaqueous systems.[29] On the other hand, a similar shift in the redox potential of a redox couple has been reported when using Li^+- and K^+-containing supporting electrolytes, due to different solvating interactions.[30] Therefore, we consider the change in the solvation structure as the major contributor to the redox potential shift, which we will further discuss using Raman spectroscopy. Compared with the 1 m LiTFSI, the CVs exhibit more of a rectangular shape at the reversal potentials (0 and 0.35 V vs Ag/Ag^+). This rectangular shape in the CVs suggests the system may have increased capacitive character.[31]

Figure 1c shows linear plots of the natural logarithm of peak current densities of $[Fe(CN)_6]^{3-}$ reduction versus the natural logarithm of scan rates. In 1 m LiTFSI, the plot exhibits a slope of 0.51, which is characteristic of a diffusion-controlled reversible faradaic process, governed by the Randles−Sevcik equation.[32] In contrast, the plot for 21 m LiTFSI exhibits a slope of 0.80, which suggests a contribution from capacitive current and/or a surface-confined redox process.[28,31]

To understand the capacitance contribution to the system, we carried out electrochemical impedance spectroscopy (EIS, Figure S1) and obtained differential capacitance C_p (Figure S2) from 1 m LiTFSI and 21 m LiTFSI using the same electrodes. Here, we note that capacitance can take a wide range of values both in experiment and simulation.[14,33] The capacitance values obtained in this work are comparable to those reported for dilute aqueous systems and ionic liquids in previous studies.[34,35] The 21 m LiTFSI system exhibits higher differential capacitance compared to the 1 m LiTFSI, supporting the presence of a greater capacitance contribution in the 21 m LiTFSI. Indeed, previous studies have utilized 21

https://dx.doi.org/10.1021/acsaem.0c01534
ACS Appl. Energy Mater. 2020, 3, 8086−8094

m LiTFSI as an electrolyte for supercapacitors.[36,37] The differential capacity at 1 Hz (Figure S2) exhibits a weak minimum at ca. −0.1 V, which is typically associated with the potential of zero charge (pzc). The pzc found here is consistent with that measured on Au in other systems.[38] While the capacitance contribution in the 21 m LiTFSI system could lead to the 0.80 slope in the linear plot of ln(current density) vs ln(scan rate), the 40 mV peak separation for the $[Fe(CN)_6]^{3-}$ reduction/oxidation peaks in the CVs suggests the presence of a surface-confined redox process.

To investigate the presence of putative surface confinement in $[Fe(CN)_6]^{3-}$ in 21 m LiTFSI, we carried out cyclic voltammetry using a Pt UME (d = 25 μm). Figure 2a shows CVs obtained in 5 mM $K_3Fe(CN)_6$ in 1 m LiTFSI and 21 m LiTFSI at a scan rate of 2 mV/s. In the CV of the 21 m LiTFSI solution, the half wave potential for $[Fe(CN)_6]^{3-}$ reduction is 0.22 V vs Ag/Ag^+, which is more positive compared to that from 1 m LiTFSI (0.13 V). This shift in reduction potential with different LiTFSI concentrations is consistent with the CVs using the Au disk electrode (Figure 1). The steady-state current density for $[Fe(CN)_6]^{3-}$ reduction is about 5 times smaller in 21 m LiTFSI compared with 1 m LiTFSI, which suggests a smaller diffusion coefficient, D_0, in the concentrated system.[24,25] More interestingly, the CV from 21 m LiTFSI exhibits an oxidation peak at 0.23 V upon the reverse positive potential sweep, which indicates the oxidation of reduced ferrocyanide $[Fe(CN)_6]^{4-}$ at this potential. In contrast, no such oxidation peak is observed in the CV of 1 m LiTSFI, which suggests that the reduced ferrocyanide $[Fe(CN)_6]^{4-}$ is not oxidized in the dilute system at the same potential. Previous studies on steady-state diffusion electrochemical processes, using UME or rotating disk electrode (RDE), have attributed the early oxidation/reduction peak in reverse potential sweep CVs to the presence of surface-adsorbed/confined redox species.[39−41] The oxidation peak at 0.23 V in the CV in the UME study, together with the small 40 mV peak separation for $[Fe(CN)_6]^{3-}$ redox in the CVs with the Au disk electrode (Figure 1b), suggests that reduced $[Fe(CN)_6]^{4-}$ is adsorbed/confined on the electrode surface in 21 m LiTFSI is oxidized at a lower potential during the reverse positive potential sweep. This adsorption/confinement is not present in the dilute 1 m LiTFSI.

We carried out additional scan rates studies using the UME (Figure S3). The adsorption density of $[Fe(CN)_6]^{4-}$ on the electrode was determined by calculating the total charge by integrating the area of the $[Fe(CN)_6]^{4-}$ oxidation peak. The adsorption/confinement of reduced $[Fe(CN)_6]^{4-}$ on the electrode surface is characteristic of the concentrated 21 m LiTFSI and thus would be induced by features specific to the electrode−electrolyte interface between the electrode surface and 21 m LiTFSI, which will be further discussed in AFM studies.

Figure 2b,c shows simulated and experimental CVs from 5 mM $K_3Fe(CN)_6$ in 1 m LiTFSI and 21 m LiTFSI. D_0 and electrochemical rate constant k^0 were derived from the simulations. The oxidation peak of $[Fe(CN)_6]^{4-}$ in 21 m LiTFSI is not considered in the simulation. For 1 m LiTFSI, the best fit to the data from the simulation yields $D_0 = 3.4 \times 10^{-6}$ cm^2/s and k^0 = 0.006 cm/s, consistent with previous studies.[42,43] For 21 m LiTFSI, the simulation yields $D_0 = 7.4 \times 10^{-7}$ cm^2/s and k^0 = 0.002 cm/s. The decrease in D_0 is attributed to the high viscosity of 21 m LiTFSI.[44] On the other hand, the decrease in k^0 could be due to differences in the $[Fe(CN)_6]^{3-}$ solvation structure, which has been reported to affect charge-transfer kinetics previously.[45]

Raman Spectroscopy. Raman spectroscopy was carried out to understand the solvation of $[Fe(CN)_6]^{3-}$ in 1 m LiTFSI and 21 m LiTFSI. Figure 3 shows the Raman spectra obtained

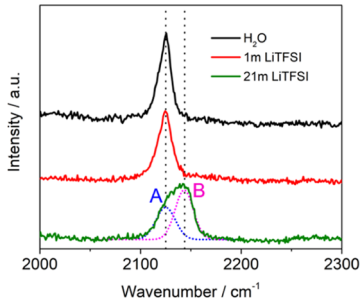

Figure 3. Raman spectra of 100 mM $K_3Fe(CN)_6$ solutions in H_2O, 1 m LiTFSI, and 21 m LiTFSI.

for 100 mM $K_3Fe(CN)_6$ in H_2O, 1 m LiTFSI, and 21 m LiTFSI. In the spectra of H_2O and 1 m LiTFSI, a peak at 2125 cm^{-1} (peak A) is observed, which is assigned to the CN stretching ν(CN) of cyanide in H_2O-solvated $[Fe(CN)_6]^{3-}$.[46] For 21 m LiTFSI, the ν(CN) peak appears asymmetric in shape and shifts to higher wavenumber. Peak fitting yields two Gaussian peaks at 2125 cm^{-1} (peak A) and 2144 cm^{-1} (peak B). The peak at 2125 cm^{-1} (peak A) corresponds to H_2O-solvated $[Fe(CN)_6]^{3-}$, as observed in H_2O and 1 m LiTFSI. The peak at 2144 cm^{-1} (peak B) is located at higher wavenumber, which suggests different $[Fe(CN)_6]^{3-}$ solvation. Previous Raman studies reported a positive shift in wavenumber for ν(CN) in $[Fe(CN)_6]^{3-}$ with addition of LiCl to the solution.[47] Given the high concentration of solvated Li^+ $[Li(H_2O)_x]^+$ in 21 m LiTFSI, the shift to 2144 cm^{-1} for CN stretch could be due to the interaction of cyanide ligand in $[Fe(CN)_6]^{3-}$ with $[Li(H_2O)_x]^+$.[9] This difference in the solvation structure is likely responsible for the change in electrochemical rate constant k^0 (Figure 2).[45,48] In addition, previous surface-enhanced Raman spectroscopy (SERS) studies have reported on $[Fe(CN)_6]^{3-}$ reduction at a markedly positive potential with the addition of LiCl, which suggests that the interaction with $[Li(H_2O)_x]^+$ could lead to the reduction of $[Fe(CN)_6]^{3-}$ at a more positive potential, as observed in our electrochemical studies (Figures 1 and 2).

AFM Force Measurements. The short-range interfacial structure in 21 m LiTFSI was measured on a Au (111)-textured surface under applied potential to compare to the electrochemical studies described earlier. Figure 4a−c shows heatmaps obtained by combining the 64 separate force−distance curves at each potential. The measured force−distance curves reveal discontinuities in the profile (a typical discontinuity marked with an arrow in Figure 4b) as layers either of ions and/or water molecules are displaced with the sharp tip, and therefore, the steps reflect the arrangement of ions and water in layers at the WiSE/electrode interface.[49] A higher force typically suggests a stronger adsorption of the molecules or ions either to the surface or to the underlying layers. The solvation structure vanishes beyond ∼2 to 3 layers at all conditions. Good reproducibility of the curves was achieved at OCP (measured to be −0.16 V) and at +0.3 V, as evidenced by the high count density on the heatmap. Although the steps were clearly resolved on individual curves at −0.4 V

https://dx.doi.org/10.1021/acsaem.0c01534
ACS Appl. Energy Mater. 2020, 3, 8086−8094

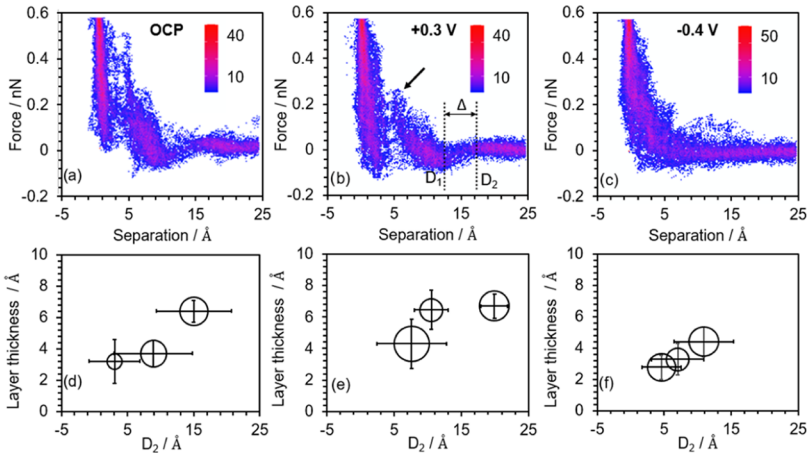

Figure 4. (a–c) Heatmaps of superposed force–separation curves measured by AFM in 21 m LiTFSI solution and (d–f) bubble diagrams with the layer thickness (Δ) as a function of the onset separation (D_2) at (a, d) OCP, (b, e) +0.3 V vs Ag/Ag^+, and (c, f) −0.4 vs Ag/Ag^+, respectively.

(Figure S4), the presence of a step was less evident when the force curves were superposed in a heatmap. The layered structure of the double layer in 21 m LiTFSI likely leads to a thinner double layer and a higher capacitance (as observed in Figure S2), as reported in a previous study on the ionic liquids.[50]

Figure 4d–f shows the bubble diagrams plotting the layer thickness as a function of step onset distance. The layer thickness (Δ) is defined as the difference of the film thickness from the onset of the step (D_2) to the end of the step (D_1), i.e., $\Delta = D_2 - D_1$, with $D_2 > D_1$. Based on both the force required to push through the layer, as well as the position of the onset, three groups of layers were identified at each potential, which are shown in Figure 4d–f. The size of the bubble is proportional to the frequency (or probability) this layer is found on the 64 force curves measured. We note that the factors influencing the layer thickness include the composition of the layer, the degree of disorder, the compressibility of the molecules and hydrated ions (at pressures as high as 0.5 GPa applied with the tip), and the possible pressure-induced dehydration of ions.[51,52] Indeed, recent MD simulations for ionic liquids suggest that compressibility of ions at high pressures can result in substantially reduced layer thickness. Thus, the layer thickness may be smaller than the actual molecular size.

At OCP, the step beginning at D_2 = 15 Å is resolved in most of the curves. The thickness of this layer ($\Delta \sim 6.7$ Å) is significantly larger than the thickness of the layers observed at closer separations (3.2 and 3.7 Å, respectively). The magnitudes of Δ values at +0.3 V (Δ = 4.3, 6.4, and 6.7 Å) are larger than that seen at OCP, while the thickness values at −0.4 V are smaller (Δ < 5 Å) than at OCP. At −0.4 V, the three resolved layers do not occur at distinct tip–surface separations, so the bubbles appear superposed along the D_2 axis. Nevertheless, the steps occur at distinct forces, which is illustrated in Figure 5.

Figure 5 is a bubble diagram of the force vs layer thickness seen at the three potentials examined here. Figure 5 also presents the effective size of $[TFSI]^-$ and hydrated Li^+, the latter based on recent MD simulations of 21 m LiTFSI in the bulk WiSE.[9] The figure shows that the species interrogated by AFM change as a function of potential. At −0.4 V, the steps are observed exhibiting a thickness Δ = 4.3 Å and then with progressively higher force Δ becomes 3.3 and 2.8 Å. The ca. 3

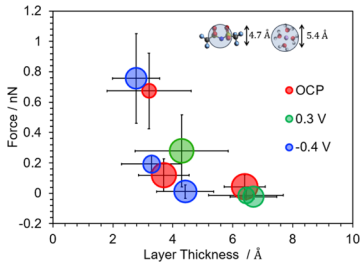

Figure 5. Bubble diagram of force vs layer thickness for 21 m LiTFSI solution on gold at OCP, +0.3 and −0.4 V. The inset shows the dimensions of the $[TFSI]^-$ anion and $Li(H_2O)_4$, for comparison.

Å features at this layer are associated with hydrated Li^+ at the interface due to the negative applied potential and the relatively small layer thickness. The reduced layer thickness relative to the effective size reported from MD simulations is likely a consequence of the dehydration of the Li^+ when it adsorbs to the surface. For example, Fenter and co-workers examined LiCl solutions and found a prominent Li^+ layer at 2.2–2.4 Å from a mica surface, followed by a less prominent layer at 5 Å from the surface, associated with partially dehydrated and highly hydrated Li^+.[52] At −0.4 V, this comparison thus suggests that $[Li(H_2O)_x]^+$ populates the layers closer to the surface. The high force (0.2 and 0.75 nN) of the two groups of layers with $\Delta \sim 3.3$ and ~2.8 Å, respectively, indicates the presence of strong Coulombic interactions. The small thickness of these layers compared to the calculated size of the $[Li(H_2O)_4]^+$ (ca. 5.4 Å) is, however, intriguing. It is possible that the layer at ~0.2 nN is associated with the partial dehydration of the adsorbed $[Li(H_2O)_x]^+$, and the surface-adsorbed Li^+ is resolved at a much higher force (0.75 nN); a dehydration-associated step has been reported for the dilute electrolytes in the SFA experiments before.[53] This phenomenon would explain the less well-defined heatmap, as shown in Figure 4c. Another source of the smaller dimension could be compression by the tip. For example, a distortion of the solvation shell induced by the AFM tip pressure and the adsorption to the electrode surface have been reported for Li^+ ions chelated to oligoether ligands with 3–4 repeating units.[54,55]

An additional feature at 4.3 Å and relatively low force is found at −0.4 V. There are several possible origins of this

https://dx.doi.org/10.1021/acsaem.0c01534
ACS Appl. Energy Mater. 2020, 3, 8086–8094

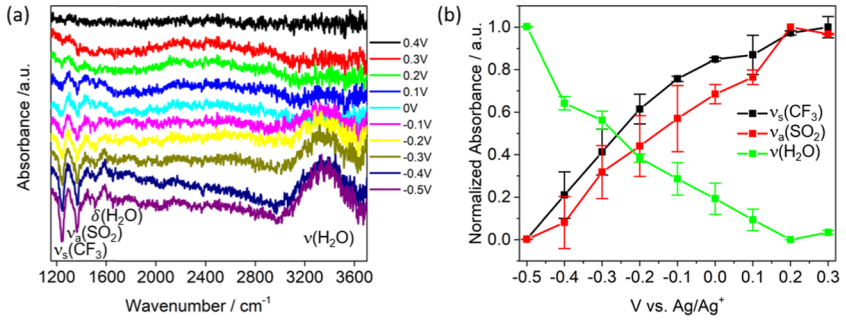

Figure 6. (a) ATR-SEIRAS spectra of 21 m LiTFSI at various potential vs Ag/Ag^+. (b) Normalized absorbance of $\nu_s(CF_3)$, $\nu_a(SO_2)$, and $\nu(H_2O)$ as a function of potential vs Ag/Ag^+. The reference spectrum was collected at 0.4 V vs Ag/Ag^+.

feature. First, we note the 4.3 Å layer thickness is close to that predicted for hydrated Li^+. The existence of a solvation layer with $\Delta \sim 4.3$ Å might indicate the presence of a second solvation layer rich in $[Li(H_2O)_x]^+$ to further counterbalance the surface potential. The two solvation layers rich in hydrated Li^+ may then reflect the so-called crowding of the multiple layers of counterions in the highly concentrated electrolytes.[56] On the other hand, previous works on $[TFSI]^-$ containing ionic liquids report that layers of ca. 4.4 Å represent layers rich in $[TFSI]^-$, very close to the 4.3 Å spacing measured here, and slightly smaller than that calculated based on the packing dimension (4.7 Å) and the van der Waals diameter (5.3 Å).[55,57,58] We note the 4.3 Å spacing is also seen at +0.3 V, where the interface is expected to be $[TFSI]^-$-rich (vide infra).

At +0.3 V, a different set of layer thickness (4.3 and 6.7 Å) is observed. At +0.3 V, $[Li(H_2O)_x]^+$ is likely repelled from the Au electrode and replaced by solvation layers rich in $[TFSI]^-$ associated with the surface. The layer thickness $\Delta = 4.3$ Å suggests that it is associated with $[TFSI]^-$, based on the discussion above. However, we cannot completely rule out the occasional presence of the cation complex, since layers of around 3 Å thickness are sometimes detected, as inferred from the large error bars on the $\Delta = 4.3$ Å layer.

Layers of thickness 6.4 and 6.7 Å are measured at +0.3 V but not at −0.4 V. This size is too large to be associated with a single cation or anion. Thus, these larger solvation layers likely correspond to the $[Li(H_2O)_x]^+([TFSI]^-)_y$ clusters. The layers composed of ion pairs have been widely reported in the ionic liquids and solutions of metal salts in the ionic liquids.[21,59−62] The presence of ion pairs suggests that the applied potential is greatly screened by the surface-adsorbed layers. The larger thickness could reflect a weaker electrostatic attraction to the Au surface. Overall, the solvation layers resolved farther from the surface will have a higher number of co-ions and will be more loosely packed because they are less strongly bound to the surface compared to the more strongly adsorbed surface layers.

Ion clusters $[Li(H_2O)_x]^+([TFSI]^-)_y$ are not detected at −0.4 V. The weakened cation−anion interaction close to the surface at negative potential might be associated with enrichment of H_2O at the interface. H_2O, in the solvation sheath of Li^+, disrupts the packing of the species near the surface and may result in the somewhat less resolved heatmap shown in Figure 4c. In contrast, $[TFSI]^-$ forms a well-ordered layer near the positively charged surface. Due to the reduced abundance of water at positive potentials, significant cation−anion pairing happens near the surface and more commensurate packing is achieved. The well-ordered structure on the cathode together with a randomized interfacial structure on the anode has been previously visualized by molecular dynamics.[13]

OCP is typically measured to be ca. −0.1 to −0.2 V. The layer thickness measured reflects an intermediate situation between the positive and negative potentials discussed above, with both $[Li(H_2O)_x]^+$ and $[Li(H_2O)_x]^+([TFSI]^-)_y$ near the surface.

Surface Vibrational Spectroscopy. To understand the change in chemical speciation in the double layer with potential, we carried out attenuated total reflectance surface-enhanced infrared absorption spectroscopy (ATR-SEIRAS). Figure 6a shows the potential-dependent ATR-SEIRAS spectra of 21 m LiTFSI obtained from an Au film deposited on μ-groove Si wafer vs Ag/Ag^+. As the potential decreases from 0.4 to −0.5 V, two peaks with negative absorbance at 1244 and 1359 cm^{-1} are observed, assigned to the CF_3 symmetric stretching $\nu_s(CF_3)$ and SO_2 asymmetric stretching $\nu_a(SO_2)$ from $[TFSI]^-$.[9,44] The negative absorbance suggests that $[TFSI]^-$ decreases in the double layer on the Au surface at more negative potentials. This result is consistent with the previous SEIRAS study.[16] In contrast, a broadband ranging from 3000 to 3600 cm^{-1} exhibits an increasing positive absorbance as the potential decreases. This band is assigned to H_2O stretching $\nu(H_2O)$, and its increase suggests an increase in H_2O content in the double layer on the Au surface at negative potentials.[63] The absorbance peak at 1590 cm^{-1} is assigned to H_2O bending $\delta(H_2O)$.[64] The 1590 cm^{-1} peak position is considered low for $\delta(H_2O)$ and is assigned to H_2O molecules with little H-bonding, consistent with the presence of solvated Li^+ $[Li(H_2O)_x]^+$ in this system.[64,65] The $\delta(H_2O)$ absorbance peak intensity also increases as the potential decreases, which is also consistent with increased H_2O in the double layer at negative potentials.

Figure 6b shows plots of normalized absorbance of $\nu_s(CF_3)$, $\nu_a(SO_2)$, and $\nu(H_2O)$ as a function of potential. As the potential decreases, $\nu_s(CF_3)$ and $\nu_a(SO_2)$ decrease in intensity while $\nu(H_2O)$ increases in intensity, indicating a switch from a $[TFSI]^-$-rich double layer at positive potentials to a H_2O-rich double layer at negative potentials.

We also carried out potential-dependent surface-enhanced Raman spectroscopy (SERS) in the $\delta(H_2O)$ region obtained from 21 m LiTFSI on a Au disk electrode (Figure S5). Consistent with the SEIRAS study, the peak intensity of $\delta(H_2O)$ also increases as the potential decreases, which suggests increased $[Li(H_2O)_x]^+$ content in the double layer at negative potentials.

The SEIRAS results support the potential-dependent AFM study. At positive potentials, $[TFSI]^-$ dominates the double

https://dx.doi.org/10.1021/acsaem.0c01534
ACS Appl. Energy Mater. 2020, 3, 8086−8094

layer and its larger size contributes to larger layer thickness in the AFM force curves. At negative potentials, H_2O replaces $[TFSI]^-$ and smaller layers are seen in AFM. The H_2O molecules are likely coordinated by Li^+, and $[Li(H_2O)_x]^+$ would compose the double layer, as suggested by the low energy of the $\delta(H_2O)$ peak at 1590 cm^{-1}.

The surface-confinement effect observed for $[Fe(CN)_6]^{3-}$ in 21 m LiTFSI is likely caused by the distinct interfacial structures at the $[Fe(CN)_6]^{3-/4-}$ redox potential (>0 V vs Ag/Ag^+). The positive potential attendant the $[Fe(CN)_6]^{3-/4-}$ redox couple would produce a $[TFSI]^-$-rich, layered, double-layer structure. The layered structure as well as the increased hydrophobicity from enhanced $[TFSI]^-$ would inhibit the diffusion of the hydrophilic $[Fe(CN)_6]^{4-}$ to the bulk leaving $[Fe(CN)_6]^{4-}$ confined near the electrode surface. A test molecule with a more negative redox potential would likely exhibit opposite behavior and this is work in progress. The effect of LiTFSI concentration on the layered structure of the double layer is also under investigation.

CONCLUSIONS

A double-layer structure is observed in the WiSE system on a (111) textured Au surface. The layered structure exhibits potential dependence, associated with the presence of different species, as inferred from spectroscopy and AFM. At negative potentials, $[Li(H_2O)_x]^+$ is enhanced at the interface. At positive potentials, $[TFSI]^-$ and $[Li(H_2O)_x]^+([TFSI]^-)_y$ clusters are dominant. The layered structure enforces a confinement effect on ferricyanide redox couple, due to its interaction with the layered interfacial structure. Our study brings new insight into understanding the double layer of WiSE and highlights an opportunity to exploit its interfacial structure properties beyond battery applications.

METHODS

All chemicals were purchased from Sigma-Aldrich and used as received.

Electrolyte Preparation. Lithium bis(trifluoromethane sulfonyl) imide (LiTFSI, 99.95%, Sigma-Aldrich) was stored in an Ar-filled glovebox, which contained <1 ppm of O_2 and <1 ppm of H_2O, before use. All electrolytes were purged with dry N_2 before measurements. Aqueous LiTFSI solutions of various molality (mol LiTFSI/kg H_2O) were prepared with Milli-Q water. 1 and 21 m solutions were prepared by dissolving LiTFSI in H_2O.

One millimolar and 5 mM potassium ferricyanide ($K_3Fe(CN)_6$, >99%, Sigma-Aldrich) solutions were prepared by diluting 20 mM $K_3Fe(CN)_6$ stock solution with 1 and 21 m LiTFSI solutions in volume ratios of 1:9 and 1:3, respectively.

Electrochemical Characterization. All electrochemical measurements were carried out using a CH Instruments 760D potentiostat (Austin, TX). A polycrystalline Au disk electrode (0.875 cm diameter) and a Pt ultramicroelectrode (UMEs, 25 μm diameter, CH Instruments, Austin, Texas) were used as working electrodes. A Au wire and a Ag wire were used as the counter and reference electrodes, respectively. Potentials are reported vs Ag/Ag^+. The polycrystalline Au disk electrode was polished mechanically, followed by rinsing, with 9.0, 3.0, 0.25, and 0.05 μm MetaDi Monocrystalline Diamond Suspension (Buehler) on a MicroCloth polishing pad (Buehler). The Au disk was then annealed with a hydrogen flame, quenched in Milli-Q water, and dried under vacuum. The Pt UME was polished mechanically, followed by rinsing, with 3.0, 1.0, 0.5, and 0.25 μm MetaDi Monocrystalline Diamond Suspension (Buehler) on a MicroCloth polishing pad (Buehler) and electrochemically in a 0.1 M HNO_3 electrolyte by sweeping the potential from 2.0 to −0.5 V (vs Ag/AgCl) for 10 cycles prior use. Electrochemical impedance spectroscopy (EIS) was performed on a Biologic potentiostat (model SP-150, France). The alternating current (AC) perturbation signal was ±10 mV and the frequency ranged from 100 to 1 MHz. Differential capacitance was derived from EC-Lab software. COMSOL Multiphysics 5.3 simulation procedures were previously described.[25]

Raman Spectroscopy and Surface-Enhanced Raman Spectroscopy (SERS). Raman spectra were obtained by using a 632.8 nm He/Ne laser and the instrumental setup described previously.[66] The spectral resolution was calculated to be 3.0−3.3 cm^{-1} using a 50 μm slit. For bulk Raman spectroscopy, the electrolytes were placed in 20 mL scintillation vials.

Surface-enhanced Raman spectroscopy (SERS) was carried out in a home-built cell described previously.[66] A polycrystalline Au disk electrode (0.875 cm diameter) was used as the working electrode. A Au wire and a Ag wire were used as the counter and reference electrodes, respectively. The Au disk was mechanically polished and annealed under the same procedure as described above. The Au disk was then electrochemically roughened in 0.1 M KCl, as previously described.[67]

Attenuated Total Reflectance Surface-Enhanced Infrared Absorption Spectroscopy (ATR-SEIRAS). Attenuated total reflectance surface-enhanced infrared absorption spectroscopy (ATR-SEIRAS) was carried out in a Nicolet Magna-IR 550 spectrometer using a home-built spectro-electrochemical cell similar to that described previously.[68] A μ-groove Si wafer (IRUBIS GmbH, Germany) is used as the internal reflectance element.[69] The Si wafer was polished for 15 min with 3 and 0.25 μm MetaDi Monocrystalline Diamond Suspension (Buehler) on a MicroCloth polishing pad (Buehler). The Si wafer was rinsed and sonicated for 15 min with Milli-Q water before and after polishing and dried under N_2. A 20 nm thick Au film was evaporated on the Si wafer with a deposition rate of 0.01 nm/s in a Temescal E-beam evaporator. The 20 nm Au film was cleaned by cycling between −0.5 and 0.9 V vs Ag/Ag^+ for 20 cycles at 20 mV/s and used as the working electrode.[70] A Au wire and a Ag wire were used as the counter and reference electrodes, respectively. A Pike Technologies VeeMAX III ATR accessory provided control over the angle of incidence. The angle of incidence is 35°. The potential-dependent spectra were collected between 0.4 and −0.5 V vs Ag/Ag^+. The resolution was 4 cm^{-1}. The reference spectrum was collected at 0.4 V vs Ag/Ag^+.

Atomic Force Microscopy (AFM). Force measurements were conducted in a JPK (Santa Barbara, CA) atomic force microscope (AFM) equipped with CSC-37 tips (MikroMasch, CA), with spring constants of ~0.6 N/m as determined by the thermal noise method and a nominal radius of ca. 20 nm.[71] The tip was exposed to UV for 20 min prior to the measurement. Au on glass samples were purchased from Phasis (Geneva, Switzerland) and were flame-annealed by the manufacturer to achieve a (111) texture. The surface was rinsed with Millipore water and ethanol, dried under N_2, and exposed to UV light for 20 min. The process was repeated twice, after which the surface was immediately mounted into the electrochemical cell. The cell was capped with a Teflon cover to minimize the exchange of water between solution and ambient air (maximum weight gain = 3.1 wt % at 33% RH). The TFSI solution was filtered by using a 200 nm pore size PTFE membrane prior to the injection into the electrochemical cell. The system was equilibrated for 20 min before force and electrochemical measurements. AFM force measurements were obtained at the open circuit potential (OCP), +0.3, and −0.4 V against a Ag pseudo reference electrode. The electrochemical potential was applied using a CHI potentiostat. The tip velocity was set at 20 nm/s. A total of 64 force curves at each potential were collected from a 500 nm × 500 nm area by dividing the area into 64 separate squares and collecting a force curve from each square.

ASSOCIATED CONTENT

Supporting Information

The Supporting Information is available free of charge at https://pubs.acs.org/doi/10.1021/acsaem.0c01534.

https://dx.doi.org/10.1021/acsaem.0c01534
ACS Appl. Energy Mater. 2020, 3, 8086−8094

EIS data, capacitance data, UME scan rate study, AFM force−separation curves, and SERS data (PDF)

AUTHOR INFORMATION

Corresponding Authors

Rosa M. Espinosa-Marzal − *Department of Civil and Environmental Engineering, University of Illinois, Urbana, Illinois 61801, United States;* orcid.org/0000-0003-3442-2511; Phone: +1-217-300-4380; Email: rosae@illinois.edu

Andrew A. Gewirth − *Department of Chemistry, University of Illinois, Urbana, Illinois 61801, United States;* orcid.org/0000-0003-4400-9907; Phone: +1-217-333-8329; Email: agewirth@illinois.edu

Authors

Ruixian Zhang − *Department of Chemistry, University of Illinois, Urbana, Illinois 61801, United States*

Mengwei Han − *Department of Civil and Environmental Engineering, University of Illinois, Urbana, Illinois 61801, United States*

Kim Ta − *Department of Chemistry, University of Illinois, Urbana, Illinois 61801, United States*

Kenneth E. Madsen − *Department of Chemistry, University of Illinois, Urbana, Illinois 61801, United States;* orcid.org/0000-0002-1336-567X

Xinyi Chen − *Department of Chemistry, University of Illinois, Urbana, Illinois 61801, United States;* orcid.org/0000-0002-6990-5233

Xueyong Zhang − *Department of Chemistry, University of Illinois, Urbana, Illinois 61801, United States*

Complete contact information is available at: https://pubs.acs.org/10.1021/acsaem.0c01534

Notes

The authors declare no competing financial interest.

ACKNOWLEDGMENTS

This work was supported as part of the Joint Center for Energy Storage Research (JCESR), an Energy Innovation Hub funded by the U.S. Department of Energy, Office of Science, Basic Energy Sciences. K.E.M. acknowledges support from the Center for Electrochemical Energy Science, an Energy Frontier Research Center funded by the U.S. Department of Energy, Office of Science, Basic Energy Science. X.C. gratefully acknowledges the support of the International Institute for Carbon Neutral Energy Research (WPI-I2CNER), sponsored by the Japanese Ministry of Education, Culture, Sports, Science and Technology. We thank Dr. Heng-Liang Wu from National Taiwan University for helpful discussions on the SEIRAS setup. We thank machine shops from the School of Chemical Sciences and Frederick Seitz Materials Research Laboratory for SEIRAS buildup. This work was partially supported by the National Science Foundation Grant NSF DMR 19-04681 (to R.M.E-M.).

REFERENCES

(1) Zhao, Q.; Stalin, S.; Zhao, C.-Z.; Archer, L. A. Designing Solid-State Electrolytes for Safe, Energy-Dense Batteries. *Nat. Rev. Mater.* **2020**, *5*, 229−252.

(2) Xu, K. Electrolytes and Interphases in Li-Ion Batteries and Beyond. *Chem. Rev.* **2014**, *114*, 11503−11618.

(3) Li, M.; Wang, C.; Chen, Z.; Xu, K.; Lu, J. New Concepts in Electrolytes. *Chem. Rev.* **2020**, 6783.

(4) Yamada, Y.; Wang, J.; Ko, S.; Watanabe, E.; Yamada, A. Advances and Issues in Developing Salt-Concentrated Battery Electrolytes. *Nat. Energy* **2019**, *4*, 269−280.

(5) Suo, L.; Borodin, O.; Gao, T.; Olguin, M.; Ho, J.; Fan, X.; Luo, C.; Wang, C.; Xu, K. "Water-in-Salt" Electrolyte Enables High-Voltage Aqueous Lithium-Ion Chemistries. *Science* **2015**, *350*, 938−943.

(6) Chen, L.; Zhang, J.; Li, Q.; Vatamanu, J.; Ji, X.; Pollard, T. P.; Cui, C.; Hou, S.; Chen, J.; Yang, C.; Ma, L.; Ding, M. S.; Garaga, M.; Greenbaum, S.; Lee, H.-S.; Borodin, O.; Xu, K.; Wang, C. A 63 m Superconcentrated Aqueous Electrolyte for High-Energy Li-Ion Batteries. *ACS Energy Lett.* **2020**, *5*, 968−974.

(7) Yamada, Y.; Furukawa, K.; Sodeyama, K.; Kikuchi, K.; Yaegashi, M.; Tateyama, Y.; Yamada, A. Unusual Stability of Acetonitrile-Based Superconcentrated Electrolytes for Fast-Charging Lithium-Ion Batteries. *J. Am. Chem. Soc.* **2014**, *136*, 5039−5046.

(8) Wang, F.; Borodin, O.; Ding, M. S.; Gobet, M.; Vatamanu, J.; Fan, X.; Gao, T.; Eidson, N.; Liang, Y.; Sun, W.; Greenbaum, S.; Xu, K.; Wang, C. Hybrid Aqueous/Non-aqueous Electrolyte for Safe and High-Energy Li-Ion Batteries. *Joule* **2018**, *2*, 927−937.

(9) Borodin, O.; Suo, L.; Gobet, M.; Ren, X.; Wang, F.; Faraone, A.; Peng, J.; Olguin, M.; Schroeder, M.; Ding, M. S.; Gobrogge, E.; von Wald Cresce, A.; Munoz, S.; Dura, J. A.; Greenbaum, S.; Wang, C.; Xu, K. Liquid Structure with Nano-Heterogeneity Promotes Cationic Transport in Concentrated Electrolytes. *ACS Nano* **2017**, *11*, 10462−10471.

(10) Zheng, J.; Tan, G.; Shan, P.; Liu, T.; Hu, J.; Feng, Y.; Yang, L.; Zhang, M.; Chen, Z.; Lin, Y.; Lu, J.; Neuefeind, J. C.; Ren, Y.; Amine, K.; Wang, L.-W.; Xu, K.; Pan, F. Understanding Thermodynamic and Kinetic Contributions in Expanding the Stability Window of Aqueous Electrolytes. *Chem* **2018**, *4*, 2872−2882.

(11) Wang, F.; Borodin, O.; Gao, T.; Fan, X.; Sun, W.; Han, F.; Faraone, A.; Dura, J. A.; Xu, K.; Wang, C. Highly Reversible Zinc Metal Anode for Aqueous Batteries. *Nat. Mater.* **2018**, *17*, 543−549.

(12) Vatamanu, J.; Borodin, O. Ramifications of Water-in-Salt Interfacial Structure at Charged Electrodes for Electrolyte Electrochemical Stability. *J. Phys. Chem. Lett.* **2017**, *8*, 4362−4367.

(13) McEldrew, M.; Goodwin, Z. A. H.; Kornyshev, A. A.; Bazant, M. Z. Theory of the Double Layer in Water-in-Salt Electrolytes. *J. Phys. Chem. Lett.* **2018**, *9*, 5840−5846.

(14) Li, Z.; Jeanmairet, G.; Méndez-Morales, T.; Rotenberg, B.; Salanne, M. Capacitive Performance of Water-in-Salt Electrolytes in Supercapacitors: A Simulation Study. *J. Phys. Chem. C* **2018**, *122*, 23917−23924.

(15) Lim, J.; Park, K.; Lee, H.; Kim, J.; Kwak, K.; Cho, M. Nanometric Water Channels in Water-in-Salt Lithium Ion Battery Electrolyte. *J. Am. Chem. Soc.* **2018**, *140*, 15661−15667.

(16) Borodin, O.; Ren, X.; Vatamanu, J.; von Wald Cresce, A.; Knap, J.; Xu, K. Modeling Insight into Battery Electrolyte Electrochemical Stability and Interfacial Structure. *Acc. Chem. Res.* **2017**, *50*, 2886−2894.

(17) Bard, A. J.; Abruna, H. D.; Chidsey, C. E.; Faulkner, L. R.; Feldberg, S. W.; Itaya, K.; Majda, M.; Melroy, O.; Murray, R. W. The Electrode/Electrolyte Interface - A Status Report. *J. Phys. Chem. A.* **1993**, *97*, 7147−7173.

(18) Wu, C. H.; Weatherup, R. S.; Salmeron, M. B. Probing Electrode/Electrolyte Interfaces in Situ by X-Ray spectroscopies: Old Methods, New Tricks. *Phys. Chem. Chem. Phys.* **2015**, *17*, 30229−30239.

(19) Han, M.; Espinosa-Marzal, R. M. Strong Stretching of Poly(ethylene glycol) Brushes Mediated by Ionic Liquid Solvation. *J. Phys. Chem. Lett.* **2017**, *8*, 3954−3960.

(20) Kim, H.; Han, M.; Bandara, S. R.; Espinosa-Marzal, R. M.; Leal, C. Mixing Oil and Water with Ionic Liquids: Bicontinuous Microemulsions under Confinement. *Soft Matter* **2019**, *15*, 9609−9613.

(21) Hayes, R.; Borisenko, N.; Tam, M. K.; Howlett, P. C.; Endres, F.; Atkin, R. Double Layer Structure of Ionic Liquids at the Au(111) Electrode Interface: An Atomic Force Microscopy Investigation. *J. Phys. Chem. C* **2011**, *115*, 6855−6863.

(22) Endres, F.; Borisenko, N.; El Abedin, S. Z.; Hayes, R.; Atkin, R. The Interface Ionic Liquid(s)/Electrode(s): In Situ STM and AFM Measurements. *Faraday Discuss.* **2012**, *154*, 221−233.
(23) Jurado, L. A.; Espinosa-Marzal, R. M. Insight into the Electrical Double Layer of an Ionic Liquid on Graphene. *Sci. Rep.* **2017**, *7*, No. 4225.
(24) Ta, K.; See, K. A.; Gewirth, A. A. Elucidating Zn and Mg Electrodeposition Mechanisms in Nonaqueous Electrolytes for Next-Generation Metal Batteries. *J. Phys. Chem. C* **2018**, *122*, 13790−13796.
(25) Ta, K.; Zhang, R.; Shin, M.; Rooney, R. T.; Neumann, E. K.; Gewirth, A. A. Understanding Ca Electrodeposition and Speciation Processes in Nonaqueous Electrolytes for Next-Generation Ca-Ion Batteries. *ACS Appl. Mater. Interfaces* **2019**, *11*, 21536−21542.
(26) Boyle, D. T.; Kong, X.; Pei, A.; Rudnicki, P. E.; Shi, F.; Huang, W.; Bao, Z.; Qin, J.; Cui, Y. Transient Voltammetry with Ultramicroelectrodes Reveals the Electron Transfer Kinetics of Lithium Metal Anodes. *ACS Energy Lett.* **2020**, *5*, 701−709.
(27) Elgrishi, N.; Rountree, K. J.; McCarthy, B. D.; Rountree, E. S.; Eisenhart, T. T.; Dempsey, J. L. A Practical Beginner's Guide to Cyclic Voltammetry. *J. Chem. Educ.* **2018**, *95*, 197−206.
(28) Bueno, P. R.; Fabregat-Santiago, F.; Davis, J. J. Elucidating Capacitance and Resistance Terms in Confined Electroactive Molecular Layers. *Anal. Chem.* **2013**, *85*, 411−417.
(29) Amatucci, G. G.; Badway, F.; DuPasquier, A. Novel Asymmetric Hybrid Cells and the Use of Pseudo-Reference Electrodes in Three Electrode Cell Characterization. In *The Electrochemical Society Proceedings Series*; S, M. G.; W, H. D., Eds.; Pennington: NJ, 2000; Vol. *94*−*24*, pp 344−352.
(30) Zhao, Y.; Yu, Z.; Robertson, L. A.; Zhang, J.; Shi, Z.; Bheemireddy, S. R.; Shkrob, I. A.; Y, Z.; Li, T.; Zhang, Z.; Cheng, L.; Zhang, L. Unexpected Electrochemical Behavior of An Anolyte Redoxmer in Flow Battery Electrolytes: Solvating Cations Help to Fight Against the Thermodynamic-Kinetic Dilemma. *J. Mater. Chem. A* **2020**, 13470.
(31) Eftekhari, A. Metrics for Fast Supercapacitors as Energy Storage Devices. *ACS Sustainable Chem. Eng.* **2019**, *7*, 3688−3691.
(32) Zhang, R.; Pan, C.; Nuzzo, R. G.; Gewirth, A. A. CoS_2 as a Sulfur Redox-Active Cathode Material for High-Capacity Non-aqueous Zn Batteries. *J. Phys. Chem. C* **2019**, *123*, 8740−8745.
(33) Vatamanu, J.; Borodin, O.; Olguin, M.; Yushin, G.; Bedrov, D. Charge Storage at the Nanoscale: Understanding the Trends from the Molecular Scale Perspective. *J. Mater. Chem. A* **2017**, *5*, 21049−21076.
(34) Raberg, J. H.; Vatamanu, J.; Harris, S. J.; van Oversteeg, C. H. M.; Ramos, A.; Borodin, O.; Cuk, T. Probing Electric Double-Layer Composition via in Situ Vibrational Spectroscopy and Molecular Simulations. *J. Phys. Chem. Lett.* **2019**, *10*, 3381−3389.
(35) Aoki, K. J.; Chen, J.; Tang, P. Double Layer Impedance in Mixtures of Acetonitrile and Water. *Electroanalysis* **2018**, *30*, 1634−1641.
(36) Bu, X.; Su, L.; Dou, Q.; Lei, S.; Yan, X. A Low-Cost "Water-in-Salt" Electrolyte for a 2.3 V High-Rate Carbon-Based Supercapacitor. *J. Mater. Chem. A* **2019**, *7*, 7541−7547.
(37) Ma, M.; Shi, Z.; Li, Y.; Yang, Y.; Zhang, Y.; Wu, Y.; Zhao, H.; Xie, E. High-Performance 3 V "Water in Salt" Aqueous Asymmetric Supercapacitors Based on VN Nanowire Electrodes. *J. Mater. Chem. A* **2020**, *8*, 4827−4835.
(38) Dickinson, K. M.; Hanson, K. E.; Fredlein, R. A. Potentials of Zero Charge and Capacitance Minima of Polycrystalline Gold in Sodium Fluoride Solutions. *Electrochim. Acta* **1992**, *37*, 139−141.
(39) Zheng, Q.; Shao, H. Correlation Between Redox Species Adsorption and Electron Transfer Kinetics of Mildly Oxidized Graphene: A Chronocoulometry and SECM Study. *Electrochem. Commun.* **2019**, *103*, 83−87.
(40) Salazar-Banda, G. R.; Eguiluz, K. I. B.; Carvalho, A. E. d.; Avaca, L. A. Ultramicroelectrode Array Behavior of Electrochemically Partially Blocked Boron-Doped Diamond Surface. *J Braz. Chem. Soc.* **2013**, *24*, 1206−1211.
(41) Szulborska, A.; Baranski, A. Kinetics and Thermodynamics of Thioglycol Adsorption on Mercury Ultramicroelectrodes. *J. Electroanal. Chem.* **1994**, *377*, 269−281.
(42) Konopka, S. J.; McDuffie, B. Diffusion Coefficients of Ferri- and Ferrocyanide Ions in Aqueous Media, Using Twin-Electrode Thin-Layer Electrochemistry. *Anal. Chem.* **1970**, *42*, 1741−1746.
(43) Pletcher, D.; Tian, Z.-Q.; Williams, D. *Developments in Electrochemistry: Science Inspired by Martin Fleischmann*; John Wiley & Sons, 2014.
(44) Yamada, Y.; Yamada, A. Review—Superconcentrated Electrolytes for Lithium Batteries. *J. Electrochem. Soc.* **2015**, *162*, A2406−A2423.
(45) Fu, C.; Xu, L.; Aquino, F. W.; Cresce, A. v.; Gobet, M.; Greenbaum, S. G.; Xu, K.; Wong, B. M.; Guo, J. Correlating Li^+-Solvation Structure and its Electrochemical Reaction Kinetics with Sulfur in Subnano Confinement. *J. Phys. Chem. Lett.* **2018**, *9*, 1739−1745.
(46) Martín-Yerga, D.; Pérez-Junquera, A.; González-García, M. B.; Perales-Rondon, J. V.; Heras, A.; Colina, A.; Hernández-Santos, D.; Fanjul-Bolado, P. Quantitative Raman Spectroelectrochemistry Using Silver Screen-Printed Electrodes. *Electrochim. Acta* **2018**, *264*, 183−190.
(47) Fleischmann, M.; Graves, P. R.; Robinson, J. The Raman Spectroscopy of the Ferricyanide/Ferrocyanide System at Gold, *β*-Palladium Hydride and Platinum Electrodes. *J. Electroanal. Chem. Interfacial Electrochem.* **1985**, *182*, 87−98.
(48) Ong, M. T.; Verners, O.; Draeger, E. W.; van Duin, A. C. T.; Lordi, V.; Pask, J. E. Lithium Ion Solvation and Diffusion in Bulk Organic Electrolytes from First-Principles and Classical Reactive Molecular Dynamics. *J. Phys. Chem. B* **2015**, *119*, 1535−1545.
(49) Lin, W.-C.; Marcellan, A.; Hourdet, D.; Creton, C. Effect of polymer−particle interaction on the fracture toughness of silica filled hydrogels. *Soft Matter* **2011**, *7*, 6578−6582.
(50) Mao, X.; Brown, P.; Červinka, C.; Hazell, G.; Li, H.; Ren, Y.; Chen, D.; Atkin, R.; Eastoe, J.; Grillo, I.; Padua, A. A. H.; Costa Gomes, M. F.; Hatton, T. A. Self-Assembled Nanostructures in Ionic Liquids Facilitate Charge Storage at Electrified Interfaces. *Nat. Mater.* **2019**, *18*, 1350−1357.
(51) Heuberger, M.; Zach, M. Nanofluidics: Structural Forces, Density Anomalies, and the Pivotal Role of Nanoparticles. *Langmuir* **2003**, *19*, 1943−1947.
(52) Lee, S. S.; Fenter, P.; Nagy, K. L.; Sturchio, N. C. Monovalent Ion Adsorption at the Muscovite (001)−Solution Interface: Relationships among Ion Coverage and Speciation, Interfacial Water Structure, and Substrate Relaxation. *Langmuir* **2012**, *28*, 8637−8650.
(53) Zachariah, Z.; Espinosa-Marzal, R. M.; Spencer, N. D.; Heuberger, M. P. Stepwise Collapse of Highly Overlapping Electrical Double Layers. *Phys. Chem. Chem. Phys.* **2016**, *18*, 24417−24427.
(54) Cook, A.; Ueno, K.; Watanabe, M.; Atkin, R.; Li, H. Effect of Variation in Anion Type and Glyme Length on the Nanostructure of the Solvate Ionic Liquid/Graphite Interface as a Function of Potential. *J. Phys. Chem. C* **2017**, *121*, 15728−15734.
(55) McLean, B.; Li, H.; Stefanovic, R.; Wood, R. J.; Webber, G. B.; Ueno, K.; Watanabe, M.; Warr, G. G.; Page, A.; Atkin, R. Nanostructure of $[Li(G_4)]TFSI$ and $[Li(G_4)]NO_3$ Solvate Ionic Liquids at HOPG and Au(111) Electrode Interfaces as a Function of Potential. *Phys. Chem. Chem. Phys.* **2015**, *17*, 325−333.
(56) Bazant, M. Z.; Storey, B. D.; Kornyshev, A. A. Double Layer in Ionic Liquids: Overscreening versus Crowding. *Phys. Rev. Lett.* **2011**, *106*, No. 046102.
(57) Carstens, T.; Gustus, R.; Höfft, O.; Borisenko, N.; Endres, F.; Li, H.; Wood, R. J.; Page, A. J.; Atkin, R. Combined STM, AFM, and DFT Study of the Highly Ordered Pyrolytic Graphite/1-Octyl-3-methyl-imidazolium Bis(trifluoromethylsulfonyl)imide Interface. *J. Phys. Chem. C* **2014**, *118*, 10833−10843.
(58) McEwen, A. B. Electrochemical Properties of Imidazolium Salt Electrolytes for Electrochemical Capacitor Applications. *J. Electrochem. Soc.* **1999**, *146*, 1687.

https://dx.doi.org/10.1021/acsaem.0c01534
ACS Appl. Energy Mater. 2020, 3, 8086−8094

(59) Atkin, R.; El Abedin, S. Z.; Hayes, R.; Gasparotto, L. H. S.; Borisenko, N.; Endres, F. AFM and STM Studies on the Surface Interaction of [BMP]TFSA and [EMIm]TFSA Ionic Liquids with Au(111). *J. Phys. Chem. C* **2009**, *113*, 13266−13272.
(60) Li, H.; Endres, F.; Atkin, R. Effect of Alkyl Chain Length and Anion Species on the Interfacial Nanostructure of Ionic Liquids at the Au(111)−Ionic Liquid Interface as a Function of Potential. *Phys. Chem. Chem. Phys.* **2013**, *15*, 14624−14633.
(61) Carstens, T.; Lahiri, A.; Borisenko, N.; Endres, F. [Py1,4]FSI-NaFSI-Based Ionic Liquid Electrolyte for Sodium Batteries: Na^+ Solvation and Interfacial Nanostructure on Au(111). *J. Phys. Chem. C* **2016**, *120*, 14736−14741.
(62) Lahiri, A.; Carstens, T.; Atkin, R.; Borisenko, N.; Endres, F. In Situ Atomic Force Microscopic Studies of the Interfacial Multilayer Nanostructure of LiTFSI−[Py1, 4]TFSI on Au(111): Influence of Li^+ Ion Concentration on the Au(111)/IL Interface. *J. Phys. Chem. C* **2015**, *119*, 16734−16742.
(63) Rieth, A. J.; Wright, A. M.; Skorupskii, G.; Mancuso, J. L.; Hendon, C. H.; Dincă, M. Record-Setting Sorbents for Reversible Water Uptake by Systematic Anion Exchanges in Metal−Organic Frameworks. *J. Am. Chem. Soc.* **2019**, *141*, 13858−13866.
(64) Petit, T.; Puskar, L.; Dolenko, T.; Choudhury, S.; Ritter, E.; Burikov, S.; Laptinskiy, K.; Brzustowski, Q.; Schade, U.; Yuzawa, H.; Nagasaka, M.; Kosugi, N.; Kurzyp, M.; Venerosy, A.; Girard, H.; Arnault, J.-C.; Osawa, E.; Nunn, N.; Shenderova, O.; Aziz, E. F. Unusual Water Hydrogen Bond Network around Hydrogenated Nanodiamonds. *J. Phys. Chem. C* **2017**, *121*, 5185−5194.
(65) Laporta, M.; Pegoraro, M.; Zanderighi, L. Perfluorosulfonated Membrane (Nafion): FT-IR Study of the State of Water with Increasing Humidity. *Phys. Chem. Chem. Phys.* **1999**, *1*, 4619−4628.
(66) Schmitt, K. G.; Gewirth, A. A. In Situ Surface-Enhanced Raman Spectroscopy of the Electrochemical Reduction of Carbon Dioxide on Silver with 3,5-Diamino-1,2,4-Triazole. *J. Phys. Chem. C* **2014**, *118*, 17567−17576.
(67) Li, X.; Gewirth, A. A. Peroxide Electroreduction on Bi-Modified Au Surfaces: Vibrational Spectroscopy and Density Functional Calculations. *J. Am. Chem. Soc.* **2003**, *125*, 7086−7099.
(68) Ataka, K.-i.; Yotsuyanagi, T.; Osawa, M. Potential-Dependent Reorientation of Water Molecules at an Electrode/Electrolyte Interface Studied by Surface-Enhanced Infrared Absorption Spectroscopy. *J. Phys. Chem. B.* **1996**, *100*, 10664−10672.
(69) Morhart, T. A.; Unni, B.; Lardner, M. J.; Burgess, I. J. Electrochemical ATR-SEIRAS Using Low-Cost, Micromachined Si Wafers. *Anal. Chem.* **2017**, *89*, 11818−11824.
(70) Ataka, K.-i.; Osawa, M. In Situ Infrared Study of Water−Sulfate Coadsorption on Gold(111) in Sulfuric Acid Solutions. *Langmuir* **1998**, *14*, 951−959.
(71) Hutter, J. L.; Bechhoefer, J. Calibration of Atomic-Force Microscope Tips. *Rev. Sci. Instrum.* **1993**, *64*, 1868−1873.

https://dx.doi.org/10.1021/acsaem.0c01534
ACS Appl. Energy Mater. 2020, 3, 8086−8094